ACS NANO

www.acsnano.org

Ultrawide-Range Wearable Pressure Sensors for High-Load Prosthetic Interfaces

Tianhao Yu,[#] Axel González Cornejo,[#] Ziheng Wang, Junsang Lee, Taewoong Park, Sbeydi Ponce Duarte, Seokkyoon Hong, Edgar Bolívar-Nieto,* and Chi Hwan Lee*

Cite This: https://doi.org/10.1021/acsnano.5c18106 Read Online

ACCESS | Metrics & More | Article Recommendations | SI Supporting Information

ABSTRACT: **Wide-range pressure sensing is essential for wearable biomedical systems operating under diverse mechanical conditions, such as prosthetic interfaces, surgical tools, and rehabilitation devices. However, current wearable pressure sensors remain limited to narrow pressure ranges (typically ≤100 kPa), restricting their use in high-pressure settings, such as prosthetic sockets. Here, we report a wearable pressure sensor with an ultrabroad detection range—from 70 Pa to 4 MPa—representing one of the widest ranges reported to date for wearable systems. The key enabling strategy is the use of poly(diallyldimethylammonium chloride) (PDDA) as a molecular binder to electrostatically anchor multiwalled carbon nanotubes within a polyurethane foam scaffold. This PDDA-assisted layer-by-layer assembly produces a stable, homogeneous, and highly compressible conductive network that preserves sensitivity across both subtle and extreme pressures. We integrated the sensor into a smart sheath for lower-limb prosthetics and demonstrated real-time pressure mapping during sitting, standing, and walking. This system provides a practical route toward continuous, high-pressure monitoring in prosthetic and other demanding wearable applications.**

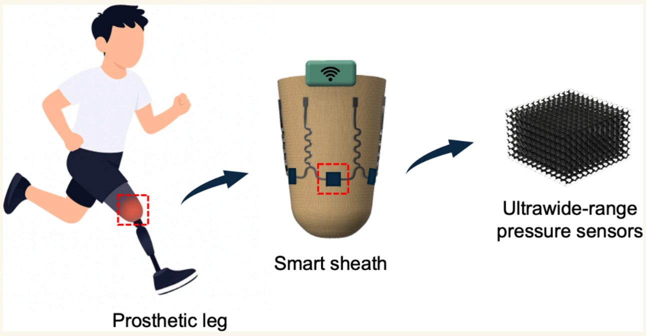

KEYWORDS: *smart textiles, wearable electronics, stretchable electronics, pressure sensors, prosthetics*

INTRODUCTION

Wide-range wearable pressure sensors are critical components in human–machine interfaces,[1−5] healthcare monitoring,[6−11] and prosthetic systems,[12−14] where the ability to detect both subtle and elevated pressures across curved, dynamic surfaces is essential. However, achieving an ultrabroad sensing range in wearable formats remains a fundamental challenge. Most reported sensors are limited to pressures below ~100 kPa,[15−21] rendering them inadequate for applications involving high mechanical loads, such as at the interface between prosthetic sockets and residual limbs. Efforts to extend the sensing range have included porous networks,[22−26] structured geometries,[27−33] and composite materials with tunable stiffness.[34−36] More recently, hybrid nanomaterial systems[37−40] and soft interlayers have been explored to enhance deformability and structural resilience. While these strategies have improved sensitivity and extended sensing ranges,[41−43] weak adhesion between conductive materials and substrates often causes delamination and degradation under repeated stress, leaving performance inadequate for reliable monitoring across both low- and high-pressure regimes. Addressing this performance gap is essential for enabling pressure sensing in domains such as prosthetic socket interfaces, where pressures can easily exceed 300 kPa during daily activities.

To address these unmet requirements, we introduce a wearable pressure sensor based on a polyurethane (PU) foam matrix functionalized with multiwalled carbon nanotubes (MWCNTs) via poly(diallyldimethylammonium chloride) (PDDA)-assisted electrostatic adsorption. This strategy enables uniform and stable dispersion of MWCNTs throughout the porous PU structure, forming reliable conductive pathways that respond sensitively to mechanical deformation. As the foam compresses, the contact area and spacing between the conductive elements change, yielding a measurable resistance shift that directly correlates with applied pressure. Leveraging this design, our sensor achieves an ultrabroad sensing range from 70 Pa to 4 MPa—spanning both gentle

Received: October 20, 2025
Revised: December 11, 2025
Accepted: December 12, 2025

ACS Publications

skin contact and the high interface pressures encountered in prosthetic socket applications. The sensor also remains stable over a broad environmental window (−20 to 120 °C, 10−90% relative humidity), indicating excellent robustness.

Indeed, the core motivation for this sensor design lies in its applicability to one of the most clinically demanding and underaddressed scenarios: monitoring interface pressure in lower-limb prosthetic sockets. In the United States alone, over 2 million individuals rely on prosthetic limbs.[13,44] And uneven pressure distribution at the socket−residual limb interface remains a leading cause of skin irritation, tissue damage, and user discomfort. Accurate, real-time pressure monitoring is essential for optimizing socket fit and preserving long-term skin health,[45−49] yet remains technically challenging due to the highly dynamic, curved, and high-pressure nature of this interface. Existing wearable sensors lack the sensing range, mechanical resilience, and conformability required to operate under such conditions. In contrast, the ultrabroad detection range and flexible structure of our sensor make it uniquely suited to this application. As a proof of concept, we integrated the sensor into a smart textile sheath designed for prosthetic sockets, enabling the continuous mapping of pressure distributions during various ambulatory activities. This system-level demonstration highlights the sensor's potential to address a long-standing unmet need in prosthetics by improving comfort, safety, and long-term quality of life for amputees.

RESULTS AND DISCUSSION

Material Characterization and Sensing Mechanism. Figure 1a illustrates the surface treatment process for the PU foam. Because of the hydrophobic nature of PU, the foam is first coated with PDDA as an adhesion promoter,[50,51] a formaldehyde-free color stabilizer used in the textile industry, making the skeleton surfaces positively charged. Then, a layer of MWCNTs is applied, which were chosen over other nanomaterials due to their exceptional electrical conductivity and mechanical robustness. With this cycle repeated three times, as shown in Figure S1a, it enhances the coating uniformity and adhesion of MWCNTs on the foam surface. Energy-dispersive spectroscopy (EDS) spectra (Figure S1b) and scanning electron microscopy (SEM) images (Figure S1c) confirm the successful coating of pristine PU foam with PDDA, as evidenced by the appearance of Cl peaks and a uniform Cl distribution. SEM images of foam with and without PDDA treatment are presented in Figure 1b for comparison, and the PDDA-treated foam shows a more uniform and stable attachment of MWCNTs, as indicated by the denser coverage in the magnified images. In contrast, foam without PDDA exhibits less uniform attachment of MWCNTs, implying weaker adhesion and potentially less consistent conductivity.

Figure 1c illustrates the mechanism of the pressure sensor, in which resistance decreases upon compression. When external pressure is applied, the foam structure deforms (left), reducing the interparticle distance between adjacent conductive pathways within the skeleton. This decrease in spacing increases the number of contact points and the probability of near-contact interactions, thereby generating new and shorter conductive paths for electron transport (center schematic). As the distance becomes sufficiently small, previously isolated conductive clusters begin to merge, enabling the formation of continuous conductive networks. This distance-driven transition toward the percolation threshold explains the pronounced reduction in resistance.[52] A simplified circuit model further illustrates this effect: in the uncompressed state, two parallel conductive paths exist, a direct path (R) and a longer three-segment path (3R), yielding an effective resistance of 0.75R. Upon compression, the MWCNT-coated skeleton forms an additional shortcut that shortens the longer path from 3R to 2R, reducing the equivalent resistance to ~0.66R. Finite element analysis (FEA) simulations of the primary current paths (defined as paths carrying over 10% of the initial current) reveal that when compressed to 60% of its initial thickness, the PU foam exhibits a significantly expanded network of conductive pathways compared to its uncompressed state (right). This expanded current pathway network corroborates the proposed mechanism of resistance reduction through the increased number of internal contacts upon compression. Figure S2a demonstrates SEM images of PU foam with different porosities (ppi, pores per inch), shown as 45 ppi, 60 ppi, and 80 ppi. As the ppi increases, the foam structure appears denser, which may influence both its mechanical properties and electrical conductivity under compression. The simulation results are consistent with the SEM images in Figure S2b, the flat foam has a uniform coating, while the deformed foam exhibits compressed and more densely packed pores. When an external force is applied to the sensor, the skeleton is compressed, and the MWCNTs successfully coated on the skeleton, as confirmed by the Raman spectrum in Figure S3a, come into closer contact,

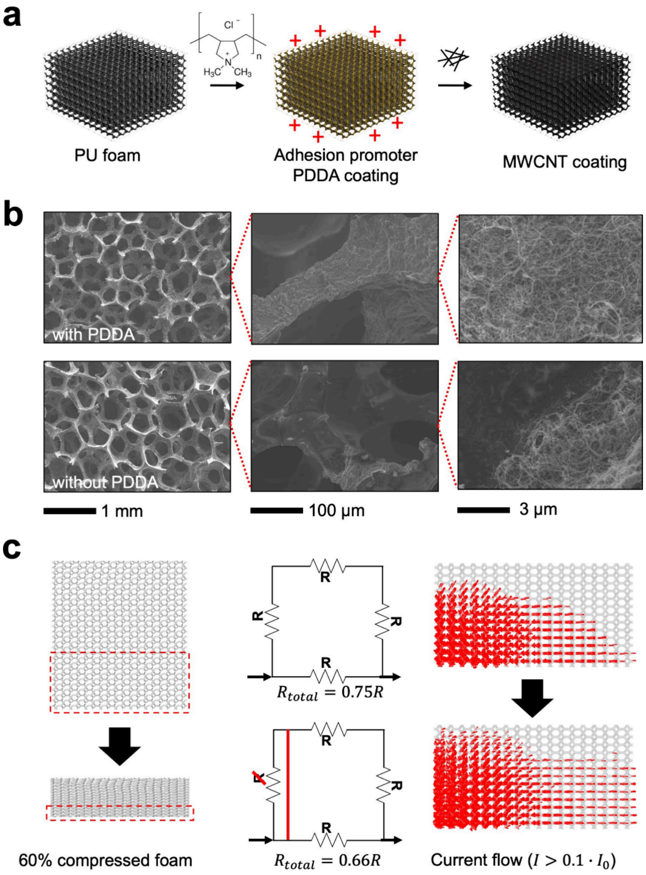

Figure 1. Material characterization and sensing mechanism. (a) PU foam coated with PDDA first and then MWCNT. (b) SEM images of PU foam coated with/without PDDA in different magnification factor. (c) FEA results of current flow paths increase upon applied pressure.

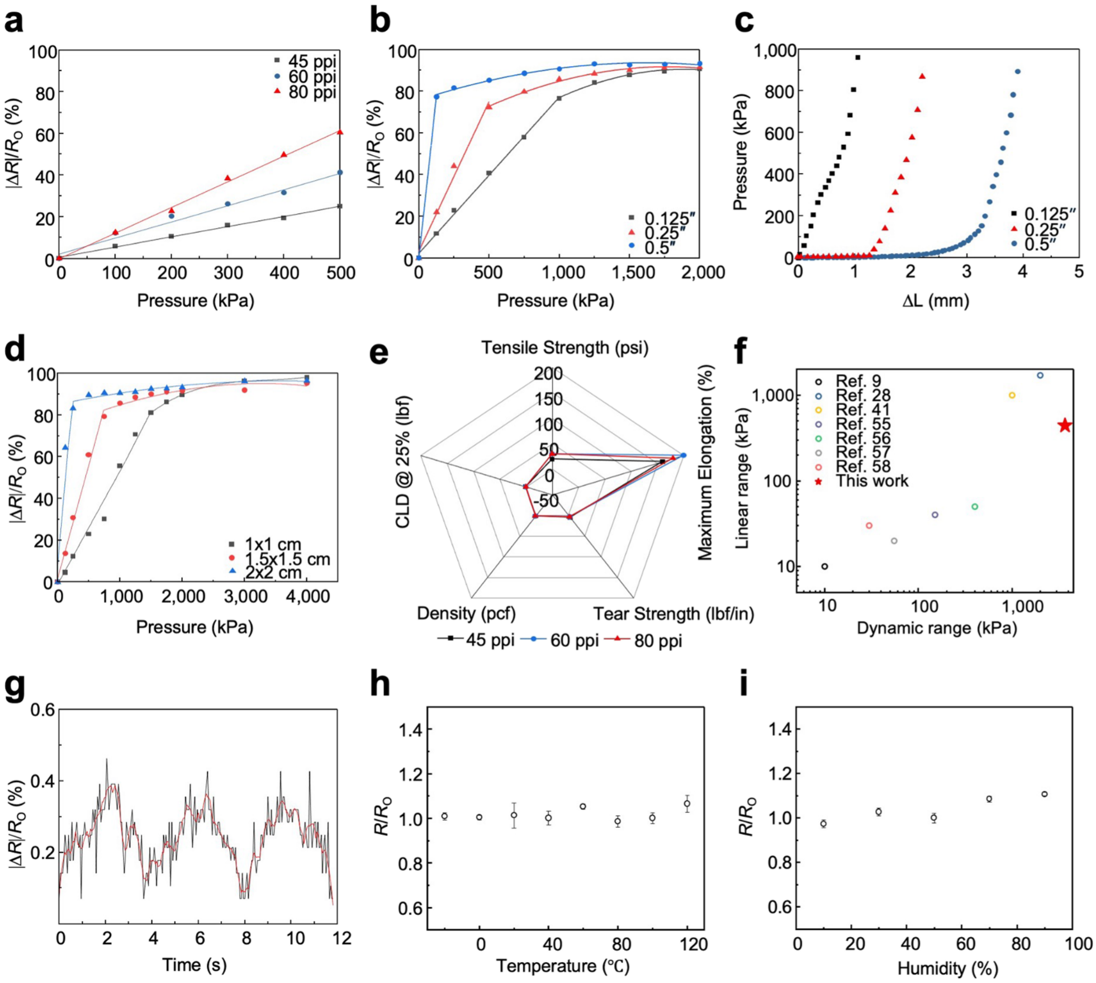

Figure 2. Structural optimization for enhanced pressure sensitivity and range. (a) Different porosity (size: 1.5 × 1.5 cm, thickness: 0.25 in.). (b) Different thickness (size: 1.5 × 1.5 cm, porosity: 80 ppi). (c) Pressure-deformation test (size: 1.5 × 1.5 cm, porosity: 80 ppi). (d) Different size (porosity: 80 ppi, thickness: 0.25 in.). (e) Mechanical properties comparison. (f) Dynamic range comparison. (g) Fractional change in resistance of the sensor under subtle pressure around 70 Pa (size: 1.5 × 1.5 cm, porosity: 80 ppi, thickness: 0.25 in.). (h) Normalized resistance under different temperatures. Error bars represent standard deviation, $n = 3$ for each group (size: 1.5 × 1.5 cm, porosity: 80 ppi, thickness: 0.25 in.). (i) Normalized resistance under different humidities. Error bars represent standard deviation, $n = 3$ for each group (size: 1.5 × 1.5 cm, porosity: 80 ppi, thickness: 0.25 in.).

forming additional conductive pathways and resulting in a decrease in electrical resistance. Benefit from the electrostatic attractions between PDDA and MWCNTs, the sensor can even withstand 10 washing cycles[53,54] (Figure S3b) without significant resistance change. Also, after being pressed under 500 kPa, the foam without PDDA shows obvious detachment (Figure S3c). The initial resistance follows an approximately normal distribution among 50 samples (Figure S4a), indicating good repeatability and low variation. Meanwhile, the pressure–resistance response curves (Figure S4b) reveal a stable and consistent performance across five randomly chosen samples, validating the reliability.

Structural Optimization for Enhanced Pressure Sensitivity and Range. Figure 2 provides a comprehensive performance characterization of the PU foam-based pressure sensor, demonstrating the effects of porosity, thickness, and size on the foam's electrical and mechanical responses to pressure. Figure 2a shows the relationship between normalized resistance change and applied pressure for PU foams with different porosities (45, 60, and 80 ppi) at a constant thickness of 0.25 in. And the pressure sensitivity (S) is defined as $S = (\Delta R/R_0)/\Delta P$, where ΔR represents the resistance change of the sensor, R_0 represents the resistance without pressure, and ΔP represents the applied pressure. The experimental setup for detecting the resistance change of the sensor is schematically shown in Figure S5. The results indicate that as the porosity increases (from 45 to 80 ppi), the sensitivity of the foam to pressure also increases from 0.0005 to 0.0012 kPa^{-1}, since a subtle pressure could largely deform the structure and create more conductive pathways in the high-porosity structure. The higher sensitivity of the 80 ppi foam observed in Figure 2a persists throughout the entire range, because prosthetic socket pressures typically operate below 500 kPa, the comparison in Figure 2a emphasizes the most relevant regime for our target application. Figure 2b presents the normalized resistance change as a function of pressure for foams with varying thicknesses (0.125″, 0.25″, and 0.5″) at a constant pore size of 80 ppi. Thicker foams (e.g., 0.5″) exhibit higher sensitivity at lower pressures, while thinner foams (e.g., 0.125″) have a more limited response range, demonstrating how thickness impacts the foam's pressure sensitivity and dynamic range. According to the pressure–deformation curve in Figure 2c, when subjected to pressure, the foam with larger thickness has a greater deformation than those with smaller thickness. The larger the thickness, the greater the deformation of the foam skeleton, the more contact of the MWCNTs on the skeleton, the more conductive pathways formed, and the greater the change of resistance.[55]

Figure 2d explores the effect of sample size on normalized resistance change under pressure, with samples of 80 ppi foam in three different dimensions (1 × 1, 1.5 × 1.5, and 2 × 2 cm). Larger samples (e.g., 2 × 2 cm) show a higher resistance change at lower pressures, which suggests that the size also affects sensitivity, potentially due to greater contact area in larger size with the same pressure source. At lower pressures (below ∼1500 kPa), the open-cell PU foam undergoes progressive compression. This deformation reduces the interparticle spacing between adjacent MWCNTs and continuously increases the number of conductive pathways. In this regime, the change in resistance is roughly proportional to the applied load, resulting in an approximately linear response. However, when the pressure exceeds ∼1500 kPa, the foam enters its densification regime. At this stage, most pores have already collapsed, and additional compression primarily causes the thickening of the cell walls rather than the formation of new conductive paths. Consequently, the incremental decrease in resistance diminishes, leading to a gradual saturation of the signal and a deviation from linearity at high pressures. In addition, the PDDA-assisted electrostatic assembly firmly anchors the MWCNTs onto the PU skeleton, preventing filler detachment under high compression, high-pressure cycling measurements from 1 to 2 MPa (Figure S6) show stable output over 1,000 cycles with negligible drift, and the hysteresis area (∼9.3% of the loading curve) confirms good reversibility even in the nonlinear densification regime. These data indicate that although the response saturates above ∼1 MPa due to foam densification, the signal remains reproducible and can be calibrated for applications requiring high-load discrimination. A radar plot in Figure 2e compares the mechanical properties of PU foams with different porosity (45, 60, and 80 ppi), evaluating parameters such as density (pounds per cubic foot), CLD (compression load deflection) at 25% deformation, tensile strength, maximum elongation, and tear strength. The 80 ppi foam shows higher tensile strength, indicating improved mechanical resilience, but it has lower maximum elongation to 60 ppi foams, showing a trade-off in properties. Taking all these findings into consideration, an 80 ppi foam with a thickness of 0.25 in. and a size of 1.5 × 1.5 cm champions the best performance. These findings illustrate the sensor's tunable sensitivity and dynamic range, making it suitable for applications requiring high flexibility and wide pressure measurement capabilities. Figure 2f compares the dynamic range and linear range of the pressure sensor developed in this study to previous works from various publications (nonexhaustive survey).[9,28,41,56−59] The dynamic range of this study is notably higher, from 70 Pa (Figure 2g) to 4 MPa, emphasizing the enhanced performance of this pressure sensor in terms of its broad measurable range. Also as shown in Figure 2h,i, the normalized resistance remains essentially constant across the tested temperature (from −20 °C up to 120 °C) and relative humidity (up to ∼90%) ranges, indicating negligible environmental drift. At high humidity levels, although PDDA and PU can absorb moisture, the resulting dimensional change is minimal compared with the large structural deformation induced during sensing. Because the dominant electrical response originates from MWCNTs contact formation rather than polymer swelling, the effect of humidity on the measured signal is negligible. This is consistent with stable behavior.

Pressure-Sensing Performance. In Figure 3, the specimens have a porosity of 80 ppi, a thickness of 0.25 in., and a size of 1.5 × 1.5 cm, unless otherwise noted. Figure 3a shows the $I-V$ (current−voltage) characteristics of the pressure sensor at various applied pressures, ranging from 1 to 1000 kPa. The sensor exhibits a linear response across all pressure levels, which indicates stable ohmic behavior with increasing pressure. As the pressure increases, the slope of the $I-V$ curve also increases, reflecting a decrease in resistance due to the increasing conductive pathways. The representative resistance profiles of the sensor under seven different applied pressures are plotted in Figure 3b. It is notable that the good correlation between responding signals and pressure levels enable the sensors to detect diverse pressure loads. As the pressure increases from 1 to 1000 kPa, the relative resistance changes increase consistently, demonstrating its ability to detect pressures over several orders of magnitude.

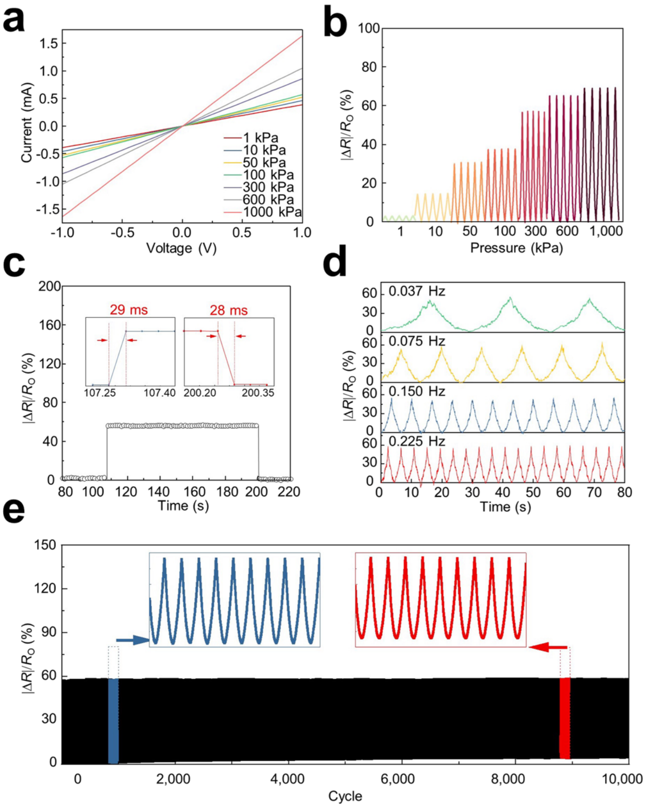

Figure 3. Pressure-sensing performance. (a) $I-V$ curves of the sensor with applied various pressures. (b) Cyclic relative resistance responses of the sensor to different pressures. (c) Respond and recovery time of the sensor during loading/unloading of 500 kPa using a linear motion stage moving at a speed of 20 mm/s. (d) Cyclic relative resistance responses of the sensor to 500 kPa at different frequencies. (e) Reliability test of the sensor through 10,000 loading/unloading cycles at a pressure of 500 kPa.

The time-response plot in Figure 3c examines the response and recovery times of the sensor under a step pressure change. The insets highlight the rapid response and recovery times, approximately 29 and 28 ms during loading/unloading of 500 kPa, respectively. This fast response indicates that the sensor is suitable for dynamic applications, where real-time pressure monitoring is essential. It is worth noting that our customized LabVIEW-based system has a maximum sampling rate of approximately 40 Hz. As a result, the measured response times are limited by this sampling interval. Here, the response time is defined as the time for the signal to reach ∼90% of its steady-state value upon loading and the recovery time as the time to return to ∼10% of baseline after unloading. Figure 3d shows the frequency response of the sensor at various compression frequencies (0.037, 0.075, 0.150, and 0.225 Hz). The sensor demonstrates consistent performance across all tested frequencies, with clear peaks corresponding to each applied frequency. This result suggests the sensor can reliably respond to cyclic loading without frequency-dependent behavior or loss of signal fidelity. Figure 3e illustrates the long-term stability and durability of the sensor under repeated cycling. The sensor undergoes 10,000 cycles of loading and unloading, with insets showing detailed views of the waveform at cycles near the beginning and end of the test. The stable values over 10,000 cycles indicate excellent durability and minimal degradation, demonstrating the sensor's suitability for applications requiring prolonged usage.

System-Level Integration and Ex Vivo Validation on an Artificial Limb. Figure 4a illustrates the application of a pressure sensor within a prosthetic setup. The smart sheath, embedded with a pressure sensor array and serpentine conductive interconnections, is positioned between the residual limb and the prosthetic socket. Since we directly modify the commercially available sheath, the existence of the pressure sensor will not compromise the intrinsic properties such as stretchability and breathability of textile. We develop a transfer-iron-on process (Movie S1) to apply conductive fabric onto the 3D curve surface of the sheath (Figure S7a) to form interconnections, nickel and copper coated fabric is first patterned by Cricut and then transferred to sheath via iron, because the force between interconnection and sheath through hot-melt polymer is stronger than the interconnection and transfer tape (Figure S7b), and the conductive interconnection is successfully left on sheath. The serpentine design enables a stretchability of 100% (Figure S8a) and durability of 10,000 cycles (Figure S8b), with imperceptible resistance change. Also, the island-bridge structure decouples the stretching and the pressure sensor; there is barely an effect of different stretching extents to the pressure sensor (Figure S8c). The system is encapsulated by a thin layer of Eco-flex to eliminate the sweat effect for a human subject test (Figure S8d). The data from the sensor are transmitted wirelessly via a data acquisition (DAQ) module and simultaneously stored on a micro SD card, allowing for real-time interface pressure monitoring in the socket of the prosthetic limb (Figures S9 and S10). This setup (Figure S11) contains two steps: (1) use elastomer (Eco-flex in this case) to mimic residual limb and (2) use the proposed system to obtain pressure data for calibration.

Figure 4b shows the ex vivo setup using an Instron machine for applying controlled loads on a prosthetic socket filled with Eco-flex, simulating the interaction between the residual limb and the socket (Movie S2). The right side illustrates the components involved, including the top load frame, adapters, femur model, and bottom load frame. This setup allows for controlled testing of the sensor's response under different load conditions. Close-up images of the smart sheath in Figure 4c demonstrate the integration of the serpentine conductive interconnection and the pressure sensor. The serpentine structure provides flexibility and stretchability, allowing it to conform to the contours of the residual limb. The images show how the sensor and interconnections are embedded within the sheath, ensuring they remain in place during wear. Figure 4d compares the pressure sensor values with those from the load cell (as ground truth) under applied loads, with a line representing the ideal $y = x$ correlation. The close alignment of the test values to the $y = x$ line indicates accuracy and reliability of the sensor in measuring applied loads, validating its effectiveness for interface pressure measurement in prosthetics. It is worth mentioning that the wireless data acquisition system can communicate with mobile application up to 10 m, and a 500 mAh lithium-ion polymer battery can support it for up to 50 h (average 9.47 mA, maximum 25.93 mA).

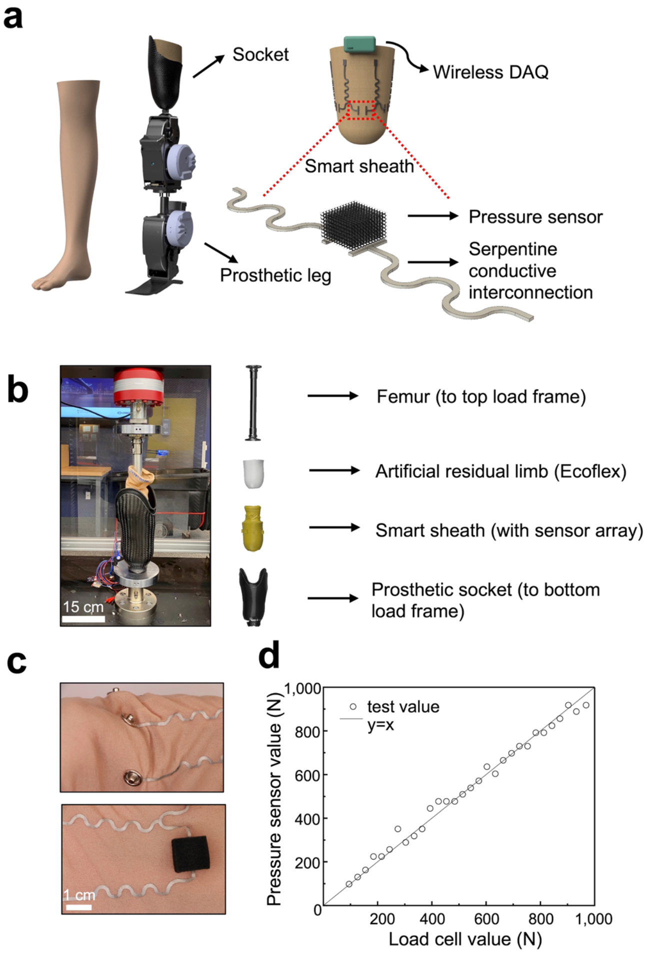

Figure 4. System-level integration and ex vivo validation on an artificial limb. (a) Schematic illustration of the smart sheath system, including stretchable serpentine conductive interconnection, pressure sensor, and a wireless DAQ device. (b) Testbed setup within an Instron tensile tester. (c) Sensor structure with metal snaps installed to facilitate electrical connectivity. (d) Pressure sensor vs load cell (ground truth validation).

Dynamic Pressure and Gait Analysis in an Individual with Transtibial Amputation. To evaluate the dynamic pressure distribution and motion patterns at the prosthetic socket interface, we integrated a wireless pressure sensing system onto the residual limb of a transtibial prosthesis user

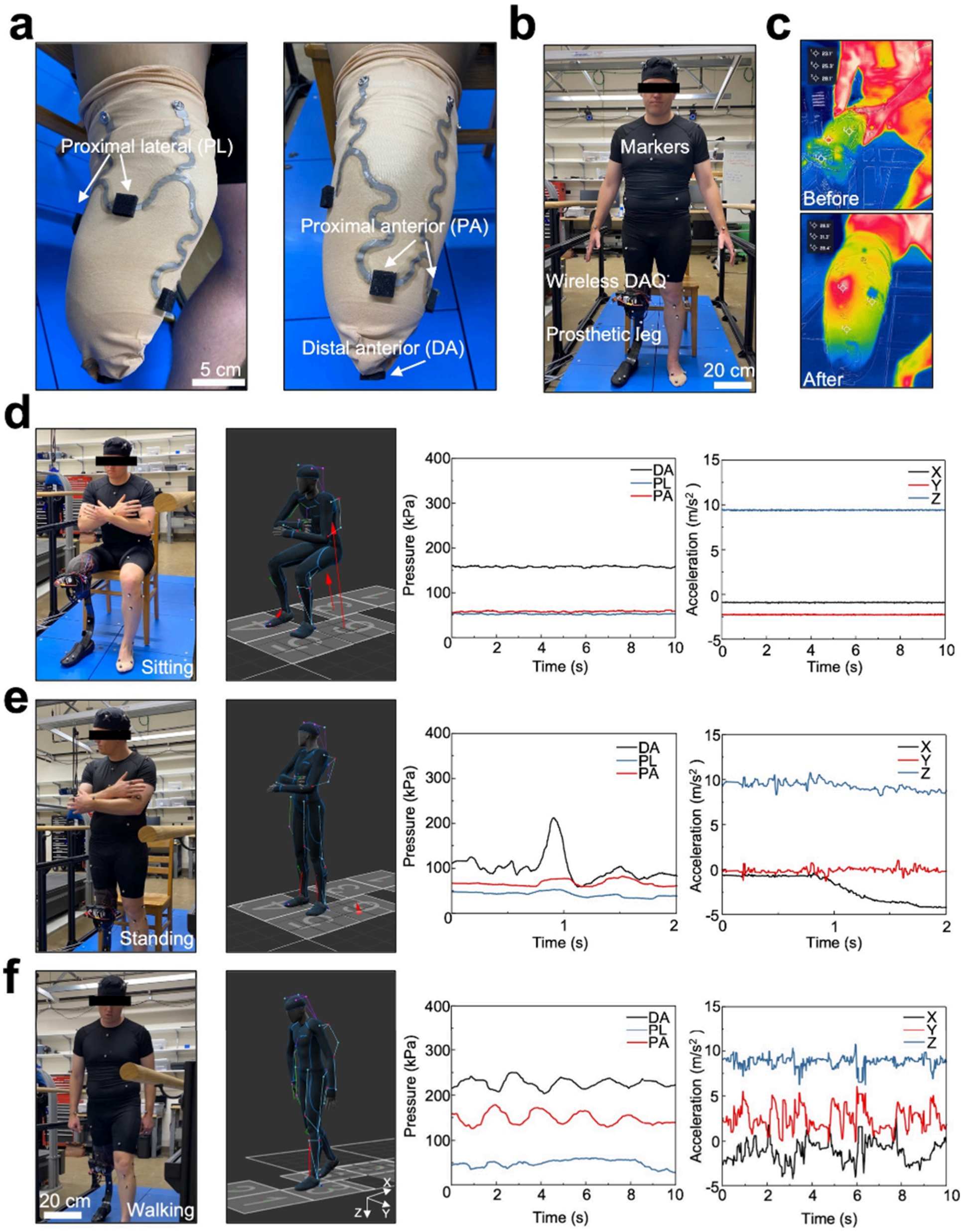

Figure 5. Dynamic pressure and gait analysis in an individual with transtibial amputation. (a) Images of a transtibial residual limb with integrated flexible pressure sensor arrays positioned at three locations: proximal lateral (PL), proximal anterior (PA), and distal anterior (DA). (b) Subject with prosthetic limb with wearable wireless DAQ system and 57 infrared markers during experimental sessions. (c) Thermal imaging of the residual limb before and after prolonged prosthetic use, indicating localized temperature variations. (d–f) Representative data during (d) sitting, (e) standing, and (f) walking activities. For each condition, synchronized data from optical motion capture, pressure sensors (DA, PA, and PL), and triaxial accelerometers (*X*, *Y*, and *Z*) are displayed. Distinct pressure distributions and acceleration profiles reflect the dynamic loading patterns and movement characteristics across different activities.

(Figure S12, Movie S3). Three pressure sensors were positioned at clinically relevant locations:[60] proximal lateral (PL), proximal anterior (PA), and distal anterior (DA) regions of the residual limb (Figure 5a). The flexible sensors were conformally attached on the sheath with conductive interconnections encapsulated by Eco-flex, where selective surface protection is used to improve durability and prevent biofouling.[61,62] To accommodate different testing scenarios, the serpentine interconnections used for on-body testing differ from those used during calibration with wider traces adopted to enhance mechanical flexibility and robustness during wear. A wearable wireless DAQ module with an accelerometer unit, and 57 infrared markers (OptiTrack) enabled real-time signal collection during activities (Figure 5b). Additionally, thermal imaging (FLIR) was performed to assess localized temperature changes before and after prolonged prosthetic use (duration is around 1 h) (Figure 5c), as well as using a bent-knee adapter (Figure S13), highlighting potential regions of heat accumulation. Importantly, no substantial heat accumulation was observed across the sensor sites during prolonged wear, except in the vicinity of the battery compartment.

During sitting, stable pressure values were observed across all sensor locations, with the DA region exhibiting the highest average pressure, ∼150 kPa (Figure 5d), while the other regions show ∼50 kPa. The corresponding acceleration data indicated minimal limb movement, consistent with the

https://doi.org/10.1021/acsnano.5c18106
ACS Nano XXXX, XXX, XXX−XXX

stationary posture. Transitioning to standing resulted in a distinct redistribution of pressure (Figure 5e), characterized by transient pressure spikes, particularly at the DA location, reflecting weight shifting and postural adjustments. The accelerometer data revealed fluctuations in the *X*-axis direction, consistent with subtle sway and muscle activity during static standing.

Walking trials demonstrated cyclic pressure variations corresponding to gait cycles (Figure 5f). The DA region consistently experienced higher peak (from ~200 to ~250 kPa) pressures relative to PA (from ~150 to ~200 kPa) and PL (~50 kPa), reflecting load transfer during the stance phase. Simultaneously recorded triaxial acceleration data captured characteristic oscillations associated with alternating stance and swing phases with pronounced fluctuations in the anterior-posterior (*Y*-axis) and vertical (*Z*-axis) directions. These combined pressure and motion data sets provide quantitative insights into the dynamic mechanical environment at the limb−socket interface during functional activities.

In contrast to commercial systems such as the Tekscan F-Scan Socket,[63,64] which rely on thin-film pressure sensors and tethered data acquisition units, our smart sheath offers wireless, multisite pressure and motion monitoring in a fully wearable format. Moreover, while F-Scan systems are typically limited to flat or semicurved surfaces and require meticulous sensor alignment, our foam-based sensor demonstrates strong durability and environmental stability and can be embedded into stretchable textile sheaths, providing a conformal and compliant interface that preserves socket geometry without requiring socket modification. The integration of synchronized triaxial accelerometry further provides complementary kinematic information that conventional pressure systems lack, enabling comprehensive, real-world gait characterization without motion constraints.

CONCLUSIONS

In this study, we developed and demonstrated a wide-range, durable, and conformal pressure-sensing system tailored to the challenging mechanical environment of prosthetic socket interfaces. By utilizing the PDDA-assisted electrostatic assembly of MWCNTs on PU foam, we obtained stable conductive networks that remain functional under high compressive stress, prolonged cyclic loading, and repeated washing cycles.

Crucially, our sensor achieves a sensing range from 70 Pa to 4 MPa. This expanded range enables accurate monitoring of pressure regimes encountered in prosthetic sockets, including peak loads up to 300 kPa during daily activities, which are often beyond the detection capabilities of piezoresistive, capacitive, or piezoelectric sensors. The ability to capture both low- and high-pressure levels in real time provides a more complete picture of the limb−socket interaction, which is essential for clinical decision-making but is largely inaccessible with existing technologies.

The integration of our sensor array into a smart sheath allows continuous wireless mapping of pressure distributions across anatomically relevant regions of the residual limb. Coupled with a wearable DAQ system and motion tracking, our platform synchronously captures both mechanical loading and limb dynamics during functional tasks such as sitting, standing, and walking. Real-world evaluation with transtibial amputees revealed region-specific pressure variations and gait-related pressure cycles, offering rich data sets that prosthetists can use to refine socket alignment, optimize load distribution, and enhance user comfort and safety.

While these results are promising, several opportunities for future improvement remain. Scaling up the sensor array to cover the full socket surface may require further miniaturization and optimization of the DAQ hardware. Larger cohort studies across diverse patient populations and prosthetic designs are essential to validate long-term clinical efficacy. Moreover, incorporating additional sensing modalities, such as shear stress, skin temperature, additional physiological signals like EMG,[65] or humidity, could provide a more comprehensive assessment of residual limb health and support personalized prosthetic management.

In summary, this work presents a robust and clinically relevant platform for next-generation wearable sensing in prosthetic care. The uniquely broad sensing range, coupled with mechanical resilience and wireless integration, directly addresses limitations of prior technologies and opens new possibilities for real-time, data-driven improvement of the prosthetic socket design and fit.

METHODS AND MATERIALS

Fabrication of Pressure Sensor. PDDA (Sigma-Aldrich, average M_w 200,000−350,000, 20 wt % in H_2O) was diluted in deionized water to obtain a 10 wt % aqueous solution. 0.25 g of MWCNTs (Cheaptubes, diameter of 10−20 nm, length of 10−30 μm) was dispersed in 100 mL of isopropyl alcohol (IPA), followed by an ultrasonication for 30 min to prepare a homogeneous dispersion. PU foam (United States Plastic Corporation) was first immersed into the PDDA solution for 5 min and dried at 60 °C. Then, the PDDA-treated foam was immersed into MWCNTs dispersion solution for 5 min and dried at 60 °C. By repeating this process in a cyclic manner and rinsed in deionized water and dried, the pressure sensor was obtained.

Characterizations of Pressure Sensor. To measure the electromechanical properties of the pressure sensor, a source meter (Keithley 2400) and a custom-built LabView code (National Instruments) were used in a two-wire configuration and testing was conducted using a mechanical testing machine (Mark-10; Willrich Precision Instruments). Microstructures were observed by using field-emission scanning electron microscopy (S-4800, Hitachi, Japan) operated at 5 kV. The Raman spectrum was measured on a spectrometer (Horiba LabRAM HR).

T-Peel Test. The adhesion between the conductive fabric, transfer tape, and sheath was quantified by using a standard T-peel test. Two identical strips (10 mm wide) were bonded together using the transfer-iron-on process. One end of each strip was clamped into the upper and lower grips of a mechanical testing machine (Mark-10; Willrich Precision Instruments), forming a “T” configuration. The peel test was performed at a constant speed of 10 mm/min, and the peel force was recorded as a function of displacement.

Fabrication of Wireless DAQ Device. Commercial software (Autodesk Eagle Version 9.6.2) was used to generate schematic diagrams and layouts for the PCB (Figure S14). The set current is determined by the following formula $I_{set} = 67.7\ \text{mV}/R_{set}$, and R_{set} is 2000 Ω in this case. The bare PCB was manufactured by OSH Park (USA). All components were purchased from Digikey Electronics (USA). A detailed bill of materials is listed in Table S1. The package size for all capacitors and resistors is 0402, and 0603 for the indicator LEDs. The bootloader (Adafruit Feather nRF52840 Express) was uploaded to the Bluetooth low-energy (BLE) system-on-chip by the serial wire debug (SWD) protocol via five reserved pads on board. Solder paste (SMDLTLFP10T5; Chip Quik) was used to attach the various surface-mounted components to the PCB, facilitated by a heat gun (Int866; Aoyue) and a hot plate (MHP30; Miniware). Figure S15a displays a detailed block diagram of the pressure monitoring system; the configuration enables wireless data transmission to any portable device using BLE protocols. The actual board size is 65 × 35 mm (Figure S15b), and the layout is detailed in Figure S15c. A container was designed using commercial 3D CAD software (Autodesk Fusion 360 Version 2.0) and was printed using a stereolithography 3D printer (Form3; Formlabs), and a textile belt (Xpand) was used to attach the container to the residual limb, as shown in Figure S15d.

Human Subject Test. The human subject provided written consent to participate in this study. The research protocol was approved by the Notre Dame Institutional Review Board, Protocol ID: 24-01-8293.

ASSOCIATED CONTENT

Supporting Information

The Supporting Information is available free of charge at https://pubs.acs.org/doi/10.1021/acsnano.5c18106.

Detailed information on the sensor fabrication, material characterization, electromechanical testing, interconnection design, wireless system architecture, experimental setups, and bill of materials used in the PCB design (PDF)

Movie S1: Fabrication process of the conductive interconnections (MP4)

Movie S2: Ex vivo validation procedures (MP4)

Movie S3: Dynamic gait analysis of an individual with transtibial amputation (MP4)

AUTHOR INFORMATION

Corresponding Authors

Edgar Bolívar-Nieto − *Department of Aerospace and Mechanical Engineering, University of Notre Dame, Notre Dame, Indiana 46556, United States*; Email: ebolivar@nd.edu

Chi Hwan Lee − *School of Mechanical Engineering, Weldon School of Biomedical Engineering, School of Materials Engineering, and Elmore Family School of Electrical and Computer Engineering, Purdue University, West Lafayette, Indiana 47907, United States*; orcid.org/0000-0002-4868-7054; Email: lee2270@purdue.edu

Authors

Tianhao Yu − *School of Mechanical Engineering, Purdue University, West Lafayette, Indiana 47907, United States*; orcid.org/0000-0001-9637-352X

Axel González Cornejo − *Department of Aerospace and Mechanical Engineering, University of Notre Dame, Notre Dame, Indiana 46556, United States*

Ziheng Wang − *School of Mechanical Engineering, Purdue University, West Lafayette, Indiana 47907, United States*

Junsang Lee − *Weldon School of Biomedical Engineering, Purdue University, West Lafayette, Indiana 47907, United States*

Taewoong Park − *Weldon School of Biomedical Engineering, Purdue University, West Lafayette, Indiana 47907, United States*

Sbeydi Ponce Duarte − *Department of Aerospace and Mechanical Engineering, University of Notre Dame, Notre Dame, Indiana 46556, United States*

Seokkyoon Hong − *Weldon School of Biomedical Engineering, Purdue University, West Lafayette, Indiana 47907, United States*; orcid.org/0009-0007-6540-0389

Complete contact information is available at: https://pubs.acs.org/10.1021/acsnano.5c18106

Author Contributions

#T.Y. and A.G.C. contributed equally to this work.

Author Contributions

T.Y. and A.G.C. contributed equally to this work. E.B. and C.H.L. conceived the concept and supervised the project. T.Y. and Z.W. designed and fabricated the smart sheath. J.L. conducted the FEA simulation. T.Y. and S.P.D. conducted the ex vivo test. T.Y. and A.G.C. conducted the human subject test. T.Y. and T.P. designed the PCB. T.Y. developed the iOS application. S.H. helped with the cutting machine. T.Y. and C.H.L. wrote the manuscript. The authors thank certified prosthetist Allison Grant for assistance with the human subject test. All authors contributed to the analysis and discussion of the data.

Notes

The authors declare no competing financial interest.

ACKNOWLEDGMENTS

The research reported in this publication was supported by the National Institute of Biomedical Imaging and Bioengineering of the National Institutes of Health under Award Number R21EB034879. The content is solely the responsibility of the authors and does not necessarily represent the official views of the National Institutes of Health. C.H.L. acknowledges support from the Leslie A. Geddes and the University Faculty Scholar Endowments.

REFERENCES

(1) Xu, C.; Chen, J.; Zhu, Z.; Liu, M.; Lan, R.; Chen, X.; Tang, W.; Zhang, Y.; Li, H. Flexible Pressure Sensors in Human−Machine Interface Applications. *Small* **2024**, *20*, No. 2306655.

(2) Yang, J. S.; Chung, M. K.; Yoo, J. Y.; Kim, M. U.; Kim, B. J.; Jo, M. S.; Kim, S. H.; Yoon, J. B. Interference-free nanogap pressure sensor array with high spatial resolution for wireless human-machine interfaces applications. *Nat. Commun.* **2025**, *16*, 2024.

(3) Cao, W.; Luo, Y.; Dai, Y.; Wang, X.; Wu, K.; Lin, H.; Rui, K.; Zhu, J. Piezoresistive Pressure Sensor Based on a Conductive 3D Sponge Network for Motion Sensing and Human−Machine Interface. *ACS Appl. Mater. Interfaces* **2023**, *15*, 3131−3140.

(4) He, F.; You, X.; Wang, W.; Bai, T.; Xue, G.; Ye, M. Recent Progress in Flexible Microstructural Pressure Sensors toward Human−Machine Interaction and Healthcare Applications. *Small Methods* **2021**, *5*, No. 2001041.

(5) Liu, W.; Xiang, F.; Mei, D.; Wang, Y. A Flexible Dual-Mode Capacitive Sensor for Highly Sensitive Touchless and Tactile Sensing in Human-Machine Interactions. *Adv. Mater. Technol.* **2024**, *9*, No. 2301685.

(6) Zhou, S.; Park, G.; Longardner, K.; Lin, M.; Qi, B.; Yang, X.; Gao, X.; Huang, H.; Chen, X.; Bian, Y.; Hu, H.; Wu, R. S.; Yue, W.; Li, M.; Lu, C.; Wang, R.; Qin, S.; Tasali, E.; Karrison, T.; Thomas, I.; Smarr, B.; Kistler, E. B.; Khiami, B. A.; Litvan, I.; Xu, S. Clinical validation of a wearable ultrasound sensor of blood pressure. *Nat. Biomed. Eng.* **2025**, *9*, 865−881.

(7) Oh, Y. S.; Kim, J. H.; Xie, Z.; Cho, S.; Han, H.; Jeon, S. W.; Park, M.; Namkoong, M.; Avila, R.; Song, Z.; Lee, S. U.; Ko, K.; Lee, J.; Lee, J. S.; Min, W. G.; Lee, B. J.; Choi, M.; Chung, H. U.; Kim, J.; Han, M.; Koo, J.; Choi, Y. S.; Kwak, S. S.; Kim, S. B.; Kim, J.; Choi, J.; Kang, C. M.; Kim, J. U.; Kwon, K.; Won, S. M.; Baek, J. M.; Lee, Y.; Kim, S. Y.; Lu, W.; Vazquez-Guardado, A.; Jeong, H.; Ryu, H.; Lee, G.; Kim, K.; Kim, S.; Kim, M. S.; Choi, J.; Choi, D. Y.; Yang, Q.; Zhao, H.; Bai, W.; Jang, H.; Yu, Y.; Lim, J.; Guo, X.; Kim, B. H.; Jeon, S.; Davies, C.; Banks, A.; Sung, H. J.; Huang, Y.; Park, I.; Rogers, J. A. Battery-free, wireless soft sensors for continuous multi-site measurements of pressure and temperature from patients at risk for pressure injuries. *Nat. Commun.* **2021**, *12*, 5008.

(8) Cheng, Y.; Zhan, Y.; Guan, F.; Shi, J.; Wang, J.; Sun, Y.; Zubair, M.; Yu, C.; Guo, C. F. Displacement-pressure biparametrically regulated softness sensory system for intraocular pressure monitoring. *Natl. Sci. Rev.* **2024**, *11*, No. nwae050.

(9) Su, Q.; Zou, Q.; Li, Y.; Chen, Y.; Teng, S. Y.; Kelleher, J. T.; Nith, R.; Cheng, P.; Li, N.; Liu, W.; Dai, S.; Liu, Y.; Mazursky, A.; Xu, J.; Jin, L.; Lopes, P.; Wang, S. A stretchable and strain-unperturbed pressure sensor for motion interference−free tactile monitoring on skins. *Sci. Adv.* **2021**, *7*, No. eabi4563.

(10) Chen, J.; Zhang, J.; Hu, J.; Luo, N.; Sun, F.; Venkatesan, H.; Zhao, N.; Zhang, Y. Ultrafast-Response/Recovery Flexible Piezoresistive Sensors with DNA-Like Double Helix Yarns for Epidermal Pulse Monitoring. *Adv. Mater.* **2022**, *34*, No. 2104313.

(11) Nie, Z.; Kwak, J. W.; Han, M.; Rogers, J. A. Mechanically Active Materials and Devices for Bio-Interfaced Pressure Sensors—A Review. *Adv. Mater.* **2024**, *36*, No. 2205609.

(12) Yang, J. C.; Mun, J.; Kwon, S. Y.; Park, S.; Bao, Z.; Park, S. Electronic Skin: Recent Progress and Future Prospects for Skin-Attachable Devices for Health Monitoring, Robotics, and Prosthetics. *Adv. Mater.* **2019**, *31*, No. 1904765.

(13) Kwak, J. W.; Han, M.; Xie, Z.; Chung, H. U.; Lee, J. Y.; Avila, R.; Yohay, J.; Chen, X.; Liang, C.; Patel, M.; Jung, I.; Kim, J.; Namkoong, M.; Kwon, K.; Guo, X.; Ogle, C.; Grande, D.; Ryu, D.; Kim, D. H.; Madhvapathy, S.; Liu, C.; Yang, D. S.; Park, Y.; Caldwell, R.; Banks, A.; Xu, S.; Huang, Y.; Fatone, S.; Rogers, J. A. Wireless sensors for continuous, multimodal measurements at the skin interface with lower limb prostheses. *Sci. Transl. Med.* **2020**, *12*, No. eabc4327.

(14) Tabor, J.; Agcayazi, T.; Fleming, A.; Thompson, B.; Kapoor, A.; Liu, M.; Lee, M. Y.; Huang, H.; Bozkurt, A.; Ghosh, T. K. Textile-Based Pressure Sensors for Monitoring Prosthetic-Socket Interfaces. *IEEE Sens. J.* **2021**, *21*, 9413−9422.

(15) Cheng, W.; Wang, X.; Xiong, Z.; Liu, J.; Liu, Z.; Jin, Y.; Yao, H.; Wong, T.-S.; Ho, J. S.; Tee, B. C. K. Frictionless multiphasic interface for near-ideal aero-elastic pressure sensing. *Nat. Mater.* **2023**, *22*, 1352−1360.

(16) Ha, K.; Zhang, W.; Jang, H.; Kang, S.; Wang, L.; Tan, P.; Hwang, H.; Lu, N. Highly Sensitive Capacitive Pressure Sensors over a Wide Pressure Range Enabled by the Hybrid Responses of a Highly Porous Nanocomposite. *Adv. Mater.* **2021**, *33*, No. 2103320.

(17) Michel, T. R.; Capasso, M. J.; Cavusoglu, M. E.; Decker, J.; Zeppilli, D.; Zhu, C.; Bakrania, S.; Kadlowec, J. A.; Xue, W. Evaluation of porous polydimethylsiloxane/carbon nanotubes (PDMS/CNTs) nanocomposites as piezoresistive sensor materials. *Microsyst. Technol.* **2020**, *26*, 1101−1112.

(18) Wang, X.; Li, H.; Wang, T.; Niu, X.; Wang, Y.; Xu, S.; Jiang, Y.; Chen, L.; Liu, H. Flexible and high-performance piezoresistive strain sensors based on multi-walled carbon nanotubes@polyurethane foam. *RSC Adv.* **2022**, *12*, 14190−14196.

(19) Chen, Z.; Liu, S.; Kang, P.; Wang, Y.; Liu, H.; Liu, C.; Shen, C. Decoupled Temperature−Pressure Sensing System for Deep Learning Assisted Human−Machine Interaction. *Adv. Funct. Mater.* **2024**, *34*, No. 2411688.

(20) Oh, J.; Yang, J. C.; Kim, J.-O.; Park, H.; Kwon, S. Y.; Lee, S.; Sim, J. Y.; Oh, H. W.; Kim, J.; Park, S. Pressure Insensitive Strain Sensor with Facile Solution-Based Process for Tactile Sensing Applications. *ACS Nano* **2018**, *12*, 7546−7553.

(21) Yang, J. C.; Kim, J.-O.; Oh, J.; Kwon, S. Y.; Sim, J. Y.; Kim, D. W.; Choi, H. B.; Park, S. Microstructured Porous Pyramid-Based Ultrahigh Sensitive Pressure Sensor Insensitive to Strain and Temperature. *ACS Appl. Mater. Interfaces* **2019**, *11*, 19472−19480.

(22) Chen, H.; Su, Z.; Song, Y.; Cheng, X.; Chen, X.; Meng, B.; Song, Z.; Chen, D.; Zhang, H. Omnidirectional Bending and Pressure Sensor Based on Stretchable CNT-PU Sponge. *Adv. Funct. Mater.* **2017**, *27*, 1604434.

(23) Oh, J.; Kim, J.; Kim, Y.; Choi, H. B.; Yang, J. C.; Lee, S.; Pyatykh, M.; Kim, J.; Sim, J. Y.; Park, S. Highly Uniform and Low Hysteresis Piezoresistive Pressure Sensors Based on Chemical Grafting of Polypyrrole on Elastomer Template with Uniform Pore Size. *Small* **2019**, *15*, No. 1901744.

(24) Liu, L.; Cai, Y.; Jiang, X.; Wang, J.; Wang, C.; Duan, J.-a. A versatile surface micro structure design strategy for porous-based pressure sensors to enhance electromechanical performance. *Chem. Eng. J.* **2024**, *490*, No. 151529.

(25) Wang, M.; Wang, G.; Xu, C.; Liu, W.; Liu, L.; Ma, Y.; Lv, W.; Guo, J. High-performance flexible porous composites based on Bioinspired gradient design for wide-range pressure monitoring. *Chem. Eng. J.* **2025**, *503*, No. 158594.

(26) Srinivasan, R.; Lavanya, J.; Sankar, A. R. Wearable Flexible Pressure Sensor Based on Nitrogen-Functionalized CNT in Melamine Foam for Human Motion Monitoring. *IEEE Access* **2024**, *12*, 194566−194579.

(27) Niu, H.; Zhang, H.; Yue, W.; Gao, S.; Kan, H.; Zhang, C.; Zhang, C.; Pang, J.; Lou, Z.; Wang, L.; Li, Y.; Liu, H.; Shen, G. Micro-Nano Processing of Active Layers in Flexible Tactile Sensors via Template Methods: A Review. *Small* **2021**, *17*, No. 2100804.

(28) Yang, R.; Dutta, A.; Li, B.; Tiwari, N.; Zhang, W.; Niu, Z.; Gao, Y.; Erdely, D.; Xin, X.; Li, T.; Cheng, H. Iontronic pressure sensor with high sensitivity over ultra-broad linear range enabled by laser-induced gradient micro-pyramids. *Nat. Commun.* **2023**, *14*, 2907.

(29) Yao, J.; Qu, C.; Chen, Z.; Zhang, Y.; Xu, Y. High-Sensitive Wearable Capacitive Pressure Sensor with Hemispherical Porous Electrode. *ACS Appl. Electron. Mater.* **2024**, *6*, 2649−2658.

(30) Chen, Z.; Qu, C.; Yao, J.; Zhang, Y.; Xu, Y. Two-Stage Micropyramids Enhanced Flexible Piezoresistive Sensor for Health Monitoring and Human−Computer Interaction. *ACS Appl. Mater. Interfaces* **2024**, *16*, 7640−7649.

(31) Jin, Y.; Xue, S.; He, Y. Flexible Pressure Sensors Enhanced by 3D-Printed Microstructures. *Adv. Mater.* **2025**, *37*, No. 2500076.

(32) Kim, J.-O.; Kwon, S. Y.; Kim, Y.; Choi, H. B.; Yang, J. C.; Oh, J.; Lee, H. S.; Sim, J. Y.; Ryu, S.; Park, S. Highly Ordered 3D Microstructure-Based Electronic Skin Capable of Differentiating Pressure, Temperature, and Proximity. *ACS Appl. Mater. Interfaces* **2019**, *11*, 1503−1511.

(33) He, J.; Wang, S.; Han, R.; Liu, Y.; Gao, W.; Bao, R.; Pan, C. Wide Detection Range Flexible Pressure Sensors Based on 3D Interlocking Structure TPU/ZnO NWs. *Adv. Funct. Mater.* **2025**, *35*, No. 2418791.

(34) Lu, Y.; Lei, T.; Qin, Y.; Wang, X. A flexible pressure sensor based on embedded cracks and stiffness-regulating layer with high detection limits and wide test ranges. *J. Mater. Sci.* **2024**, *35*, 110.

(35) Jia, K.; Zhu, H.; Ke, Y.; Wang, D.; Ming, X.; Li, M.; Zhong, W.; Wang, D. Variable Stiffness Flexible Wearable Pressure Sensors with Dual-Mode Switching Sensitivity and Working Pressure Range. *ACS Appl. Electron. Mater.* **2024**, *6*, 3865−3873.

(36) Moeinnia, H.; Agron, D. J.; Ganzert, C.; Schubert, L.; Kim, W. S. Wireless pressure monitoring system utilizing a 3D-printed Origami pressure sensor array. *npj Flexible Electron.* **2024**, *8*, 21.

(37) Zhang, L.; Liu, X.; Zhong, M.; Zhou, Y.; Wang, Y.; Yu, T.; Xu, X.; Shen, W.; Yang, L.; Liu, N.; Wei, D.; Liu, Z. Micro-nano hybrid-structured conductive film with ultrawide range pressure-sensitivity and bioelectrical acquirability for ubiquitous wearable applications. *Appl. Mater. Today* **2020**, *20*, No. 100651.

(38) Stevens, M.; Yun, G.; Hasan, T. Porous Conductive Hybrid Composite with Superior Pressure Sensitivity and Dynamic Range. *Adv. Funct. Mater.* **2024**, *34*, No. 2309347.

(39) Guo, X.; Liu, T.; Tang, Y.; Li, W.; Liu, L.; Wang, D.; Zhang, Y.; Zhang, T.; Zhu, X.; Guan, Y.; Li, X.; Chen, Y.; Wu, X.; Xiao, G.; Wang, X.; Zhang, R.; Wang, D.; Mai, Z.; Hong, W.; Hong, Q.; Zhao, Y.; Zhang, Y.; Wang, M.; Yan, F.; Xing, G. Bioinspired Low Hysteresis Flexible Pressure Sensor Using Nanocomposites of Multiwalled Carbon Nanotubes, Silicone Rubber, and Carbon Nanofiber for Human−Computer Interaction. *ACS Appl. Nano Mater.* **2024**, *7*, 15626−15639.

(40) Dai, H.; Thostenson, E. T. Large-Area Carbon Nanotube-Based Flexible Composites for Ultra-Wide Range Pressure Sensing and

Spatial Pressure Mapping. *ACS Appl. Mater. Interfaces* **2019**, *11*, 48370−48380.

(41) Xu, J.; Li, H.; Yin, Y.; Li, X.; Cao, J.; Feng, H.; Bao, W.; Tan, H.; Xiao, F.; Zhu, G. High sensitivity and broad linearity range pressure sensor based on hierarchical in-situ filling porous structure. *npj Flexible Electron.* **2022**, *6*, 62.

(42) Kong, H.; Song, Z.; Xu, J.; Qu, D.; Bao, Y.; Wang, W.; Wang, Z.; Zhang, Y.; Ma, Y.; Han, D.; Niu, L. Untraditional Deformation-Driven Pressure Sensor with High Sensitivity and Ultra-Large Sensing Range up to MPa Enables Versatile Applications. *Adv. Mater. Technol.* **2020**, *5*, No. 2000677.

(43) Kim, S.; Amjadi, M.; Lee, T.-I.; Jeong, Y.; Kwon, D.; Kim, M. S.; Kim, K.; Kim, T.-S.; Oh, Y. S.; Park, I. Wearable, Ultrawide-Range, and Bending-Insensitive Pressure Sensor Based on Carbon Nanotube Network-Coated Porous Elastomer Sponges for Human Interface and Healthcare Devices. *ACS Appl. Mater. Interfaces* **2019**, *11*, 23639−23648.

(44) Rich, T. L.; Voss, G.; Fairhurst, S.; Matsumoto, M.; Brielmaier, S.; Koester, K.; Netoff, T. I.; Hansen, A. H.; Ferguson, J. E. Feasibility testing of a novel prosthetic socket sensor system. *Disabil. Rehabil.* **2023**, *45*, 2374−2381.

(45) Ferreira, A.; Correia, V.; Mendes, E.; Lopes, C.; Vaz, J. F. V.; Lanceros-Mendez, S. Piezoresistive Polymer-Based Materials for Real-Time Assessment of the Stump/Socket Interface Pressure in Lower Limb Amputees. *IEEE Sens. J.* **2017**, *17*, 2182−2190.

(46) Laszczak, P.; McGrath, M.; Tang, J.; Gao, J.; Jiang, L.; Bader, D. L.; Moser, D.; Zahedi, S. A pressure and shear sensor system for stress measurement at lower limb residuum/socket interface. *Med. Eng. Phys.* **2016**, *38*, 695−700.

(47) Wheeler, J.; Mazumdar, A.; Marron, L.; Dullea, K.; Sanders, J.; Allyn, K. *A Pressure and Shear Sensing Liner for Prosthetic Sockets*. In 2016 38th Annual International Conference of the IEEE Engineering in Medicine and Biology Society (EMBC), 2016. .

(48) Swanson, E. C.; Weathersby, E. J.; Cagle, J. C.; Sanders, J. E. Evaluation of Force Sensing Resistors for the Measurement of Interface Pressures in Lower Limb Prosthetics. *J. Biomech. Eng.* **2019**, *141*, 1010091.

(49) Yang, G.; Zheng, X.; Li, J.; Chen, C.; Zhu, J.; Yi, H.; Dong, X.; Zhao, J.; Shi, L.; Zhang, X.; Qin, Y.; Gu, Z.; Li, Z. Schottky Effect-Enabled High Unit-Area Capacitive Interface for Flexible Pressure Sensors. *Adv. Funct. Mater.* **2024**, *34*, No. 2401415.

(50) Guo, X.-J.; Xue, C.-H.; Li, M.; Li, X.; Ma, J.-Z. Fabrication of robust, superhydrophobic, electrically conductive and UV-blocking fabrics via layer-by-layer assembly of carbon nanotubes. *RSC Adv.* **2017**, *7*, 25560−25565.

(51) Peng, L.; Guo, R.; Lan, J.; Jiang, S.; Wang, X. Microwave-assisted coating of silver nanoparticles on bamboo rayon fabrics modified with poly(diallyldimethylammonium chloride). *Cellulose* **2016**, *23*, 2677−2688.

(52) Sultana, S.; Rahaman, M.; Chandan, M. R. Enhancing EMI Shielding Efficiency of Polyurethane Foam by Incorporating MWCNT-Decorated Hollow Glass Microspheres. *ACS Omega* **2025**, *10*, 2314−2326.

(53) Cho, S.; Chang, T.; Yu, T.; Gong, S. L.; Lee, C. H. Machine embroidery of light-emitting textiles with multicolor electroluminescent threads. *Sci. Adv.* **2024**, *10*, No. eadk4295.

(54) Chang, T.; Akin, S.; Cho, S.; Lee, J.; Lee, S. A.; Park, T.; Hong, S.; Yu, T.; Ji, Y.; Yi, J.; Gong, S. L.; Kim, D. R.; Kim, Y. L.; Jun, M. B.-G.; Lee, C. H. In Situ Spray Polymerization of Conductive Polymers for Personalized E-textiles. *ACS Nano* **2023**, *17*, 22733−22743.

(55) Ji, C.; Zhang, Q.; Jing, Z.; Liu, Y.; Han, D.; Wang, J.; Zhang, W.; Sang, S. Highly Sensitive Wearable Flexible Pressure Sensor Based on Conductive Carbon Black/Sponge. *IEEE Trans. Electron Devices* **2021**, *68*, 5198−5203.

(56) Wang, X. m.; Tao, L. q.; Yuan, M.; Wang, Z. p.; Yu, J.; Xie, D.; Luo, F.; Chen, X.; Wong, C. Sea urchin-like microstructure pressure sensors with an ultra-broad range and high sensitivity. *Nat. Commun.* **2021**, *12*, 1776.

(57) Cao, K.; Wu, M.; Bai, J.; Wen, Z.; Zhang, J.; Wang, T.; Peng, M.; Liu, T.; Jia, Z.; Liang, Z.; Jiang, L. Beyond Skin Pressure Sensing: 3D Printed Laminated Graphene Pressure Sensing Material Combines Extremely Low Detection Limits with Wide Detection Range. *Adv. Funct. Mater.* **2022**, *32*, No. 2202360.

(58) Wang, G.; Wang, M.; Zheng, M.; Ebo, B.; Xu, C.; Liu, Z.; He, L. Thermoplastic Polyurethane/Carbon Nanotube Composites for Stretchable Flexible Pressure Sensors. *ACS Appl. Nano Mater.* **2023**, *6*, 9865−9873.

(59) Hong, S. Y.; Oh, J. H.; Park, H.; Yun, J. Y.; Jin, S. W.; Sun, L.; Zi, G.; Ha, J. S. Polyurethane foam coated with a multi-walled carbon nanotube/polyaniline nanocomposite for a skin-like stretchable array of multi-functional sensors. *NPG Asia Mater.* **2017**, *9*, No. e448.

(60) Ko, S.-T.; Asplund, F.; Zeybek, B. A Scoping Review of Pressure Measurements in Prosthetic Sockets of Transfemoral Amputees during Ambulation: Key Considerations for Sensor Design. *Sensors.* **2021**, *21* (15), 5016.

(61) Chang, T.; Akin, S.; Kim, M. K.; Murray, L.; Kim, B.; Cho, S.; Huh, S.; Teke, S.; Couetil, L.; Jun, M. B.; Lee, C. H. A Programmable Dual-Regime Spray for Large-Scale and Custom-Designed Electronic Textiles. *Adv. Mater.* **2022**, *34*, No. 2108021.

(62) Lee, J. C.; Kim, S. Y.; Song, J.; Jang, H.; Kim, M.; Kim, H.; Choi, S. Q.; Kim, S.; Jolly, P.; Kang, T.; Park, S.; Ingber, D. E. Micrometer-thick and porous nanocomposite coating for electrochemical sensors with exceptional antifouling and electroconducting properties. *Nat. Commun.* **2024**, *15*, 711.

(63) Paternò, L.; Truppa, L.; Ibrahimi, M.; Rosini, E.; Gruppioni, E.; Ricotti, L.; Menciassi, A. Quantitative analysis of interface pressures in transfemoral prosthetic sockets. *Prosthet. Orthot. Int.* **2024**, *48*, 176.

(64) Ibarra Aguila, S.; Sánchez, G. J.; Sauvain, E. E.; Alemon, B.; Fuentes-Aguilar, R. Q.; Huegel, J. C. Interface Pressure System to Compare the Functional Performance of Prosthetic Sockets during the Gait in People with Trans-Tibial Amputation. *Sensors.* **2020**, *20* (24), 7043.

(65) Oh, B.; Lim, Y.-S.; Ko, K. W.; Seo, H.; Kim, D. J.; Kong, D.; You, J. M.; Kim, H.; Kim, T.-S.; Park, S.; Kwon, D.-S.; Na, J. C.; Han, W. K.; Park, S.-M.; Park, S. Ultra-soft and highly stretchable tissue-adhesive hydrogel based multifunctional implantable sensor for monitoring of overactive bladder. *Biosens. Bioelectron.* **2023**, *225*, No. 115060.

https://doi.org/10.1021/acsnano.5c18106